Journal of Materials Science: Materials in Electronics (2019) 30:5284–5296
https://doi.org/10.1007/s10854-019-00828-w

Core–shell g-C_3N_4@$Zn_{0.5}Cd_{0.5}S$ heterojunction photocatalysts with high photocatalytic activity for the degradation of organic dyes

Shuyan Qi[1] · Depeng Wang[1] · Yadong Zhao[1] · Huanyan Xu[1]

Received: 23 October 2018 / Accepted: 28 January 2019 / Published online: 13 February 2019

Abstract
The core-shell g-C_3N_4@$Zn_{0.5}Cd_{0.5}S$ heterojunction photocatalysts with excellent photocatalytic performance were synthesized via a simple co-precipitation hydrothermal method. The photocatalytic performance of the g-C_3N_4@$Zn_{0.5}Cd_{0.5}S$ was significantly increased by the heterojunction structure, which improved the separation and mobility of the photogenerated carriers. The highest degradation efficiency was for the 50% g-C_3N_4@$Zn_{0.5}Cd_{0.5}S$ (99%), and its degradation rate was 15.7 which was 3.7 times those of the pure g-C_3N_4 and $Zn_{0.5}Cd_{0.5}S$, respectively. The catalyst band gap gradually decreased with the increasing content of g-C_3N_4. The capture agent experiments revealed that the main active substances in the degradation process are h^+ and $O_2^{-\cdot}$. The photocatalytic activity remained at 95% after 4 cycles showing good light stabilities. This study provided a simple method for synthesizing the g-C_3N_4/ZnCdS heterojunctions with an excellent photocatalytic property.

1 Introduction

Semiconductor photocatalytic degradation is a new type wastewater treatment technology for solving environmental pollution. Metal sulfides (ZnS, CdS, et al.) are a type of photocatalyst showing a superior performance. Their main disadvantages are a wide energy band, easy photo-corrosion decomposition and poor catalytic stability [1, 2]. For example, the bandgap of ZnS is 3.77 eV [3], which is too high to effectively utilize visible light [4]. Nonetheless, the band gap can be adjusted by doping, such as a large content of Cd^{2+} can clearly decrease the band gap of $Zn_xCd_{1-x}S$ [5, 6]. The $Zn_xCd_{1-x}S$ as a typical alloyed chalcogenide semiconductor, shows good and adjustable absorption characteristics in the visible region [7, 8]. Wang et al. [9]. reported the photocatalytic degradation efficiency of $Zn_{0.2}Cd_{0.8}S$ to RhB of 60%, which was significantly higher than that of ZnS and CdS. However, the low stability and photocatalytic efficiency of $Zn_xCd_{1-x}S$ still need to be improved [10]. Generally, the heterojunction structure is considered to be an efficient method. The heterojunction structure can effectively reduce the photo-generated electron–hole recombination probability, enlarge the photo-response range, and improve the photo-corrosion performance of metal sulfides [11–13]. For example, Zhao et al. [14] synthesized a $Zn_xCd_{1-x}S$/Zn–Al layered double hydroxide (LDH). The photocatalytic efficiency of the $2Zn_{0.2}Cd_{0.8}S$/Zn–Al was 82%, which was 89.5% and 50.32% higher than that of $Zn_{0.2}Cd_{0.8}S$ and Zn–Al LDH, respectively. Wu et al. [15] reported that the photocatalytic degradation of the $Zn_{0.5}Cd_{0.5}S$-MWCNT heterojunction was 85% and the photocatalyst still had about an 80% efficiency after three recoveries.

Most of the valence bands (VBs) and conduction bands (CBs) of the metal sulfides match with g-C_3N_4 (The VB and CB potentials are 1.5 eV and − 1.2 eV, respectively), and they can be coupled to form the heterojunction structure catalysts [5]. It was found that the g-C_3N_4/CdS and g-C_3N_4/ZnS heterojunctions can enhance the visible light response range, reduce the photo-generated carries recombination and improve the photocatalytic efficiency [16, 17]. The photocatalytic degradation efficiencies of the CdS/g-C_3N_4 and ZnS/g-C_3N_4 heterojunctions to Methyl Orange (MO) were higher than those of the pure CdS, ZnS and g-C_3N_4. Usually, the flaky g-C_3N_4 is significantly stacked, inducing the nanoparticles of the metal sulfides to only disperse on the surface of the bulk g-C_3N_4 [18, 19]. This stacked structure results in a smaller contact area between the metal sulfide and g-C_3N_4, while the core–shell structure can form a coating, thus increasing the contact area between the metal sulfide and g-C_3N_4, which benefits the hole (h^+) of $Zn_{0.5}Cd_{0.5}S$

✉ Shuyan Qi
qishuyan10@163.com

[1] School of Materials Science and Engineering, Harbin University of Science and Technology, Harbin 150040, China

more easily transfer to g-C_3N_4. The core–shell structuring is beneficial to increasing the separation and migration of the photogenerated carriers, reducing the photocorrosion effect and enhancing the light stability.

In this study, we synthesized the core–shell structure of g-C_3N_4@$Zn_{0.5}Cd_{0.5}S$. The hole (h^+) of $Zn_{0.5}Cd_{0.5}S$ more easily transfered to g-C_3N_4 due to g-C_3N_4 with a lower potential and more stable chemical property. The nanoblocks of the g-C_3N_4 surface displayed a negatively charged nature [20, 21], thus Zn^{2+} and Cd^{2+} could be adsorbed on the surface and coat the g-C_3N_4 forming the core–shell heterojunction via a simple co-precipitation-hydrothermal method. The g-C_3N_4@$Zn_{0.5}Cd_{0.5}S$ reduced the disadvantages of the low visible light response range and high photoelectron-hole recombination probability.

2 Experiment

2.1 Preparation of g-C_3N_4

The pyrolysis was used to prepare g-C_3N_4. Weighed 6 g of melamine, calcined at 500 °C for 4 h with the heating rate was 5 °C/min, and then g-C_3N_4 was fully grinded.

2.2 Preparation of $Zn_{0.5}Cd_{0.5}S$ and g-C_3N_4@$Zn_{0.5}Cd_{0.5}S$

The g-C_3N_4 was prepared by heating 6 g of melamine at 550 °C for 2 h in a muffle furnace at the a heating rate of 5 °C/min. After natural cooling, the obtained sample was sufficiently ground. The $Zn_{0.5}Cd_{0.5}S$ and g-C_3N_4@$Zn_{0.5}Cd_{0.5}S$ were synthesized via the method according to Wu et al. [20]. The g-C_3N_4@$Zn_{0.5}Cd_{0.5}S$ was synthesized as follows: 1.5 mmol $Zn(Ac)_2{\cdot}2H_2O$ and 1.5 mmol $Cd(Ac)_2{\cdot}2H_2O$ were mixed in 30 ml of deionized water and stirred for 30 min.

The obtained g-C_3N_4 (0.06 g, 0.18 g, 0.3 g, 0.42 g, 0.54 g) was added to the above solution according to the mass percentages, and ultrasonically treated for 50 min. Three mmol Na_2S was dissolved in 30 ml of deionized water at a rate of 1 drop/s and stirred for 4 h. The mixed solution was then transferred to a Teflon-lined reactor and heated at 120 °C for 12 h. Finally, the precipitate was washed three times with deionized water and absolute ethanol, then dried at 70 °C for 12 h to obtain different compound ratios of g-C_3N_4@$Zn_{0.5}Cd_{0.5}S$, labelled as 10-CN@ZCS, 30-CN@ZCS, 50-CN@ZCS, 70-CN@ZCS and 90-CN@ZCS.

2.3 Characterization techniques

The crystal phase of the photocatalyst was analyzed by X-ray diffraction (XRD, D/MAX-3B, 2θ = 10–80, Cu-Kα, 40 kV, 30 mA).The surface morphologies of the samples were observed by a scanning electron microscope (SEM, FEI Sirion 200, operating voltage set at 20 KV) and a transmission electron microscope (TEM, JEOL JEM-2010, electron acceleration voltage of 200 KV).The recombination of the photo-generated carriers was tested using a photoluminescence spectrumeter (PL, RF-5301PC, Shimadzu, Japan). Test the chemical information of the sample using X-ray photoelectron spectroscopy (XPS XSAM-800). The fourier transform infrared (FT-IR) spectra of the samples were measured by a Nicolet IS10 infrared spectrometer. The UV–Vis DRS was a USB 4000 UV diffuse reflectance spectrometer from Ocean Optics USA. The three-electrode system was used to test the photocurrent and AC impedance. A 0.2 M Na_2SO_4 solution was used as the conductive solution, and a 300 W Xe lamp was used to intermittently irradiate the conductive surface of the ITO glasses. The electrochemical workstation model was the French Bioroy VMP3 workstation.

2.4 Photocatalytic experiment

Photocatalytic experiments were carried out in a self-assembled photoreactor at room temperature. A 0.1 g sample of the g-C_3N_4@$Zn_{0.5}Cd_{0.5}S$ was added to the 10 mg/L MB solution, then the suspension stirred for 1 h in the dark, A sample was taken every 30 min, the absorbance measured, and its adsorption performance calculated. The solution was then subjected to photocatalytic methylene blue (MB) and tested 25 cm from a 500 W gx-2500 Xenon source, and samples were taken every 30 min to determine the absorbance. The absorption of the resulting clear solutions at λmax = 664 nm was evaluated using a 722 spectrophotometer and the decolorization rate of the dye was calculated by the following formula:

$$D(\%) = \frac{C_0 - C_t}{C_0} \times 100\%$$

where C_0 is the initial concentration of the dye and C_t is the concentration of the dye at a particular time during the experiment.

3 Results and discussion

3.1 XRD characterization

Figure 1 is the XRD pattern of the CN@ZCS heterojunction structure with different g-C_3N_4 composition ratios. Comparing the JCPDF cards, the composition consists of g-C_3N_4 and $Zn_{0.5}Cd_{0.5}S$. There are 27.17°, 44.68° and 53.15° diffraction peaks of $Zn_{0.5}Cd_{0.5}S$ related to the standard cubic

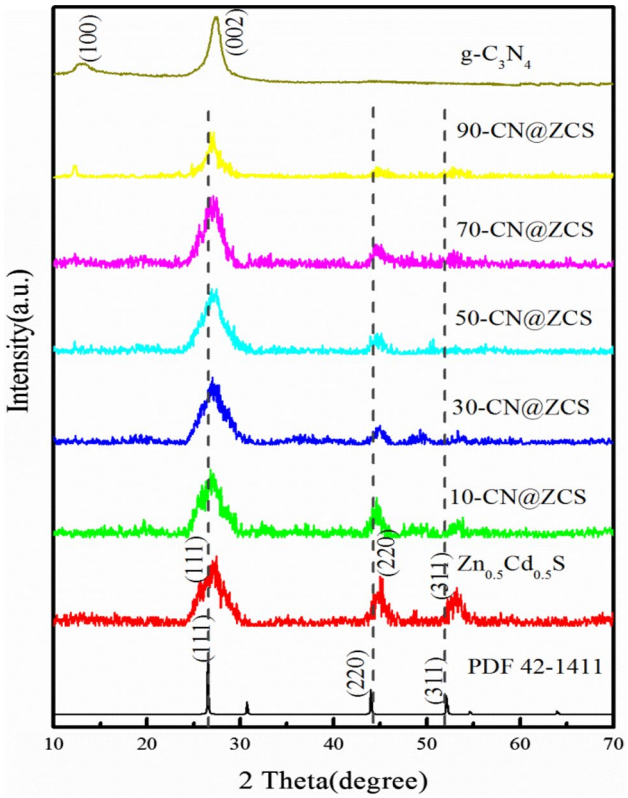

Fig. 1 XRD patterns of different CN@ZCS quality ratios

blende structure of CdS (PDF 42-1411), corresponding to its (111), (220) and (311) crystal faces, respectively. The three diffraction peaks all move toward a large angle, induced by the ionic radius of Zn (0.74 Å) being slightly smaller than that of Cd (0.97 Å). According to the Hume-Rothery rule [22], the ionic radius ratio of Zn^{2+} and Cd^{2+} is less than 15%, which means that the difference in electronegativity is low. Moreover, CdS and ZnS are both cubic sphalerite. Thus, Zn^{2+} is allowed to enter the main lattice of CdS, resulting in a lattice contraction with the diffraction peak shifting to a greater angle [8, 23].

The g-C_3N_4 has two characteristic diffraction peaks at 13.05° and 27.59°, corresponding to its (100) and (002) crystal faces, respectively. The diffraction peak at 27.59° belongs to the interlayer stacking of aromatic compounds, which is a characteristic peak specific to graphite structures. The diffraction peak at 13.05° is the characteristic peak of the melon-like substance, which is formed by the 3-s-triazine structure of the in-plane repeating unit [24, 25]. With the ratio of the g-C_3N_4 increasing, the diffraction peaks of the $Zn_{0.5}Cd_{0.5}S$ (220) and (311) crystal faces gradually decrease, and the (100) crystal plane strength of g-C_3N_4 gradually increases. Since the diffraction peak of the g-C_3N_4 (002) crystal plane overlaps with the $Zn_{0.5}Cd_{0.5}S$(111) crystal plane diffraction peak, the diffraction peaks of g-C_3N_4 (002) in the CN@ZCS hetero-structure are not detected, which is consistent with previous reports [26, 27].

3.2 Morphology analysis

It can be seen from Fig. 2a, the particles size of $Zn_{0.5}Cd_{0.5}S$ is 75 nm and g-C_3N_4 is a layer structure with a rough surface and a thickness of about 100–150 nm. Figure 2c, d show that 50-CN@ZCS obviously has a core–shell structure. The $Zn_{0.5}Cd_{0.5}S$ uniformly coats the surface of g-C_3N_4. The core diameter is 40–80 nm and the thickness of the shell is about 20 nm. The HRTEM picture shows a lattice fringe of 0.327 nm, corresponding to the (111) crystal surface of $Zn_{0.5}Cd_{0.5}S$. The lattice fringe of g-C_3N_4 is too weak to be detected. The synthesizing process of the 50-CN@ZCS core–shell heterojunction is shown in Fig. 2e. When the g-C_3N_4 is mixed with Zn^{2+} and Cd^{2+}, the Zn^{2+} and Cd^{2+} can be adsorbed by the g-C_3N_4 due to the negative charge of g-C_3N_4 in the neutral solution [20]. The lamellar g-C_3N_4 gradually shrinks into a nanoparticle during the nucleating process of $Zn_{0.5}Cd_{0.5}S$ due to the action of the $Zn_{0.5}Cd_{0.5}S$ package [21, 28]. Finally, a 50-CN@ZCS core–shell heterojunction is formed.

Elemental mapping (Fig. 3a–f) and EDS spectrum (Fig. 3g) detected C, N, Zn, Cd and S elements in the 50-CN@ZCS. The elemental mapping results also show that the C, N, Zn, Cd and S elements are uniformly distributed in the 50-CN@ZCS. The solubility product constant of ZnS (2.93×10^{-25}) is much higher than that of CdS (8.0×10^{-27}). Consequently, the reaction rate between Cd and S during faster than that of Zn and S in the nucleation process, so that the Zn content is lower than that of Cd. In summary, the formation of a 50-CN/ZCS heterojunction photocatalyst can be demonstrated.

3.3 FI-IR analysis

To further verify the functional groups in the 50-CN/ZCS heterojunction, we performed infrared tests on g-C_3N_4, $Zn_{0.5}Cd_{0.5}S$ and 50-CN/ZCS, and the results are shown in Fig. 4. There are four characteristic absorption peaks in the pure $Zn_{0.5}Cd_{0.5}S$ solid solution. The characteristic peak at 626 cm^{-1} belongs to the Zn–S bond, and the characteristic peak at 1130 and 1556 cm^{-1} belongs to the Cd–S bond stretching vibration and bending vibration absorption [17, 19], and the characteristic peak at 933 cm^{-1} should be attributed to the S-O bond, indicating that $Zn_{0.5}Cd_{0.5}S$ is oxidized to some extent during the hydrothermal process [28]. For g-C_3N_4, the absorption peak at 809 cm^{-1} corresponds to the bending vibration characteristic absorption of the triazine cyclic compound, and the absorption peak at 1200 ~ 1650 cm^{-1} corresponds to the C–N and C=N bond stretching characteristics of the aromatic heterocyclic

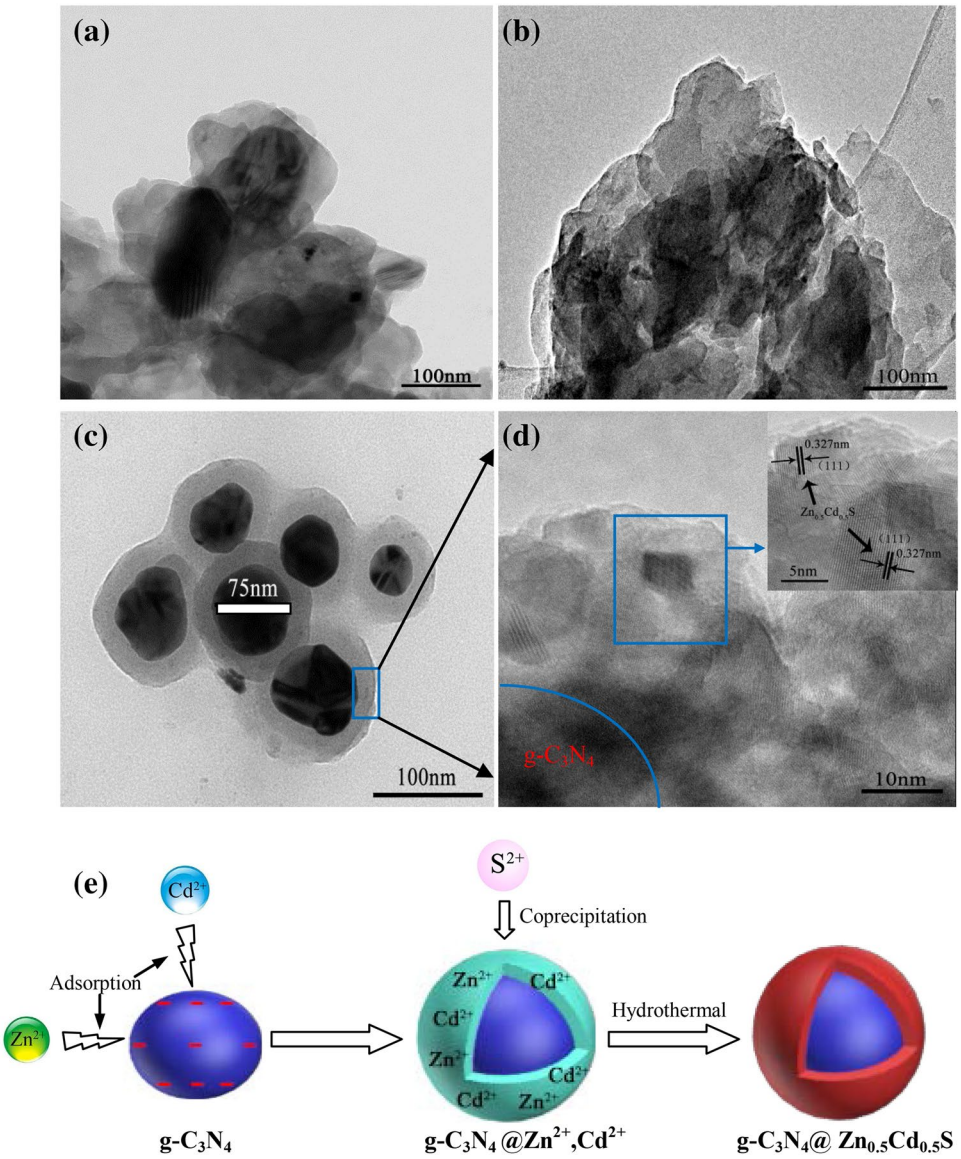

Fig. 2 The TEM images of **a** $Zn_{0.5}Cd_{0.5}S$, **b** g-C_3N_4, and **c** 50-CN@ZCS, **d** HRTEM images of 50-CN@ZCS and **e** 50-CN@ZCS synthesis mechanism diagram

compounds in g-C_3N_4 [18, 20]. The absorption peak of 50-CN/ZCS can correspond to the absorption peak of g-C_3N_4, the absorption peak of $Zn_{0.5}Cd_{0.5}S$ is weak, and the absorption peak at 50-CN/ZCS is not shown, indicating that there is no covalent bond between the g-C_3N_4 and $Zn_{0.5}Cd_{0.5}S$ nanoparticles. In addition, for all the samples, an absorption peak appeared at 3000–3800 cm^{-1}, which may be related to the stretching vibration of the N–H group in the aromatic group and the O-H stretching vibration of the adsorbed water molecule. In summary, the formation of a 50-CN/ZCS heterojunction photocatalyst can be demonstrated.

3.4 XPS analysis

The composition and chemical environment of each element in the sample can be detected by X-ray photoelectron spectroscopy (XPS). Figure 5a shows the xps measurement spectrum of a 50-CN@ZCS photocatalyst. The results show that 50-CN@/ZCS consists of C, N, Cd, Zn and S elements. As shown in Fig. 5b, the peaks of C1s are at 283.7 eV and 287.38 eV, wherein the peak at 283.7 eV is generally considered to be graphitic carbon or sp^2 C–N, and the peak at 287.38 eV is the thiazine ring (C_3N_3) unit or heptazine N–C=N of the (C_6N_7) unit [29]. The binding energy peak

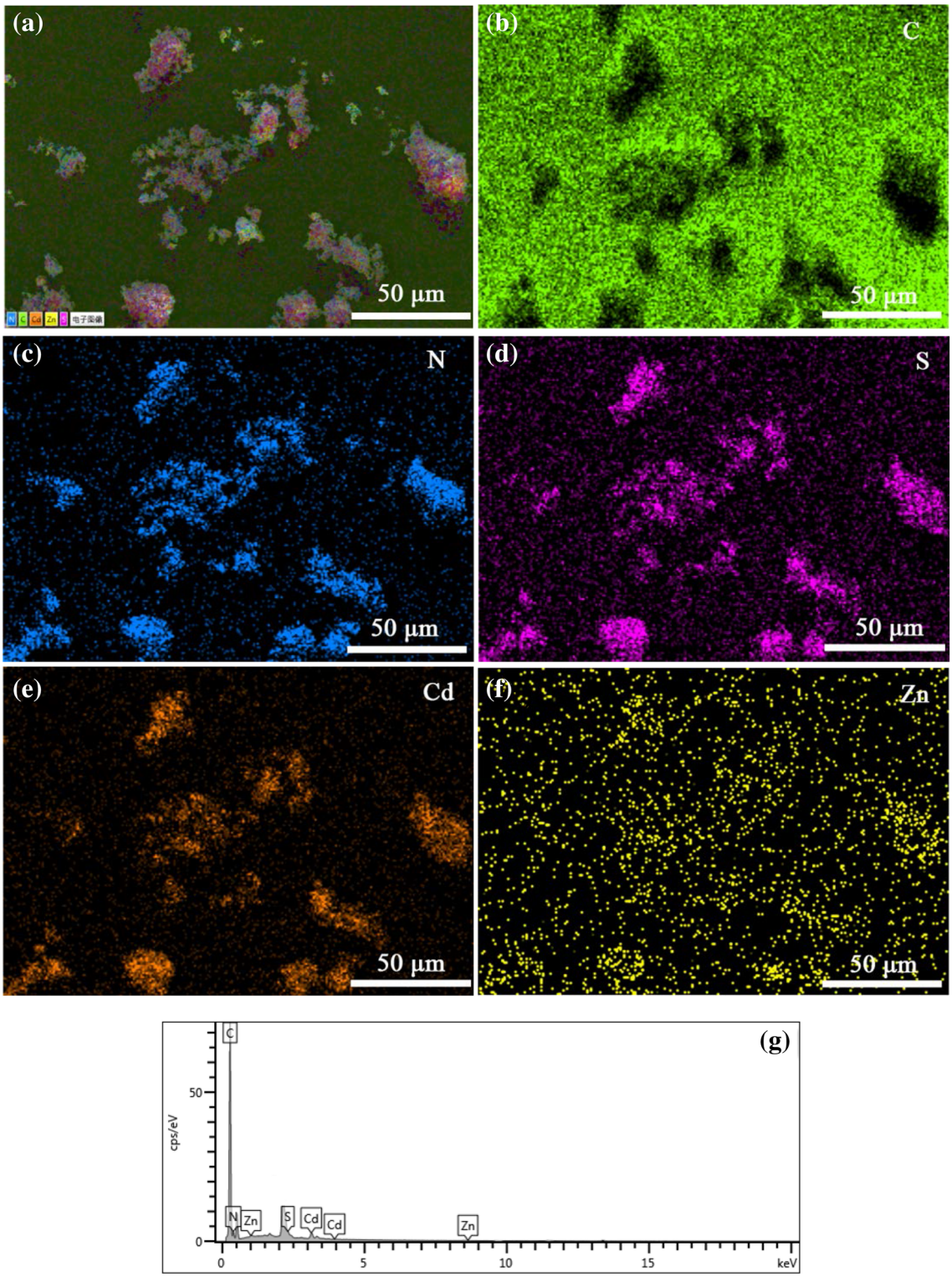

Fig. 3 Elemental mapping and EDS spectra of 50-CN@ZCS

spectrum of N 1 s of 50-CN@ZCS in Fig. 5c can be divided into two peaks, wherein the peak with the binding energy of 397.79 eV is assigned to the sp^2 hybridized N atom (C–N=C), and the peak of 403.85 eV belongs to the tertiary N species ($N–(C)_3$) groups. Figure 5d, e are xps spectra of the Cd 3*d* and Zn 2*p* orbitals, respectively. Among them, the

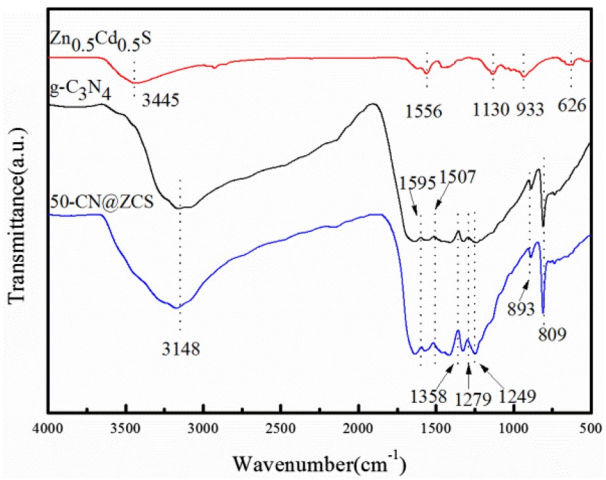

Fig. 4 FT-IR spectra of pure g-C_3N_4, $Zn_{0.5}Cd_{0.5}S$ and 50-CN@ZCS

binding energy of the Cd 3*d* orbital is located at 403.83 eV and 410.58 eV, and the binding energy of the Zn 2*p* orbital is located at 1020.6 eV and 1043.74 eV, which is obviously different from the combination of the pure ZnS and CdS at the corresponding orbit. This again confirms that the prepared catalyst is not a mixture of pure ZnS and CdS, but a metal complex sulfide $Zn_{0.5}Cd_{0.5}S$, and the interaction between metals leads to a difference in the binding energy [30]. Figure 5f shows that the binding energy of the S 2*p* orbital in 50-CN@ZCS is located at 161.4 eV, indicating the presence of a metal-S bond, and the valence state of sulfur is S^{2-}. In addition to the metal-S bond, sulfur also exhibits another form of existence with a binding energy at 167.54 eV, which is attributed to the C-S bond formed between g-C_3N_4 and ZnCdS. In summary, there is a strong interaction between g- C_3N_4 and $Zn_{0.5}Cd_{0.5}S$.

4 Photocatalytic performance and mechanism

4.1 Photocatalytic performance

The photocatalytic performance of the CN@ZCS catalyst is analyzed without adjusting the pH of the MB solution. The adsorption and photocatalytic decolorization rate curves of MB are shown in Fig. 6a.

In the adsorption stage, the decolorization rates of the g-C_3N_4, $Zn_{0.5}Cd_{0.5}S$ and 50-CN@ZCS to MB are 6.19%, 16.63% and 34.9%, respectively. The results depend of the specific surface areas of g-C_3N_4, $Zn_{0.5}Cd_{0.5}S$ and 50 CN@ZCS,which are 4.7477 m^2/g, 40.276 m^2/g and 55.561 m^2/g, respectively. Similarly, the adsorption rates of all the CN@ZCS heterojunction materials also are higher than that of g-C_3N_4 and $Zn_{0.5}Cd_{0.5}S$. In a liquid phase photocatalytic reaction, the adsorption to target the contaminants on the surface of the catalyst is a prerequisite for the photocatalytic degradation [31]. The higher adsorption can enrich the pollutants on the surface of the liquid phase [32]. Thus, the active sites in the catalyst have a higher contact ratio with the target pollutants to improve the catalytic efficiency.

In the photocatalytic stage, the degradation rates of all the CN@ZCS heterojunction materials for the MB are greater than 90% and the photocatalytic degradation rate of 50-CN@ZCS for MB reached 99.9%. All of them are higher than $Zn_{0.5}Cd_{0.5}S$ (85.67%) and g-C_3N_4 (35.5%) alone. This can contribute to the heterojunction structure of the $Zn_{0.5}Cd_{0.5}S$ and g-C_3N_4. The heterojunction reduces the forbidden band width, enhances the visible light absorption capacity and promotes the effective separation of the photogenerated electrons-holes. The photocatalytic properties of ZnS or CdS directly dispersed on carbon nitride are compared, as shown in Table 1, indicating that this core–shell structure effectively improves its photocatalytic performance.

The photocatalytic activity of CN@ZCS is quantified by the quasi-first-order kinetic model $-\ln\frac{C_t}{C_0} = k_1 t$ [33], as shown in Fig. 6b. C_0, C_t and K_1 are the original concentration of the dye solution, the concentration at *t* (min) and the quasi-first-order reaction rate constant (min^{-1}) [34], respectively. It was found that all three curves show a good linear relationship ($R^2 > 0.97$), and the reaction rate constant of 50-CN@ZCS to MB is 0.033 min^{-1}, which is 15.7 times and 3.6 times higher than those of g-C_3N_4 and $Zn_{0.5}Cd_{0.5}S$, respectively. The results show that the CN@ZCS heterojunction structure can significantly improve the photocatalytic degradation efficiency.

4.2 Absorption spectrum

In order to further confirm the mechanism of the photocatalytic process, the UV absorption was carried out, as shown in Fig. 7. The peaks at 293 nm and 664 nm indicate the MB absorption. During the adsorption process the two absorption peaks of MB decrease, indicating that the concentration of MB is reduced. After 60 min of photocatalysis, the absorption peak of MB at 664 nm is blue-shifted, the intensity decreased after 240 min, and the absorption peak at 664 nm almost disappeared, indicating that eventually MB decomposes into CO_2 and H_2O by 50-CN@ZCS.

4.3 UV–Vis DRS analysis

Figure 8a is the UV–Vis spectrum of different ratios of that composite CN@ZCS, which directly reflects the light absorption characteristics of the prepared photocatalyst. The absorption band edges of $Zn_{0.5}Cd_{0.5}S$ and g-C_3N_4 are about 510 nm and 450 nm, respectively, and the absorption

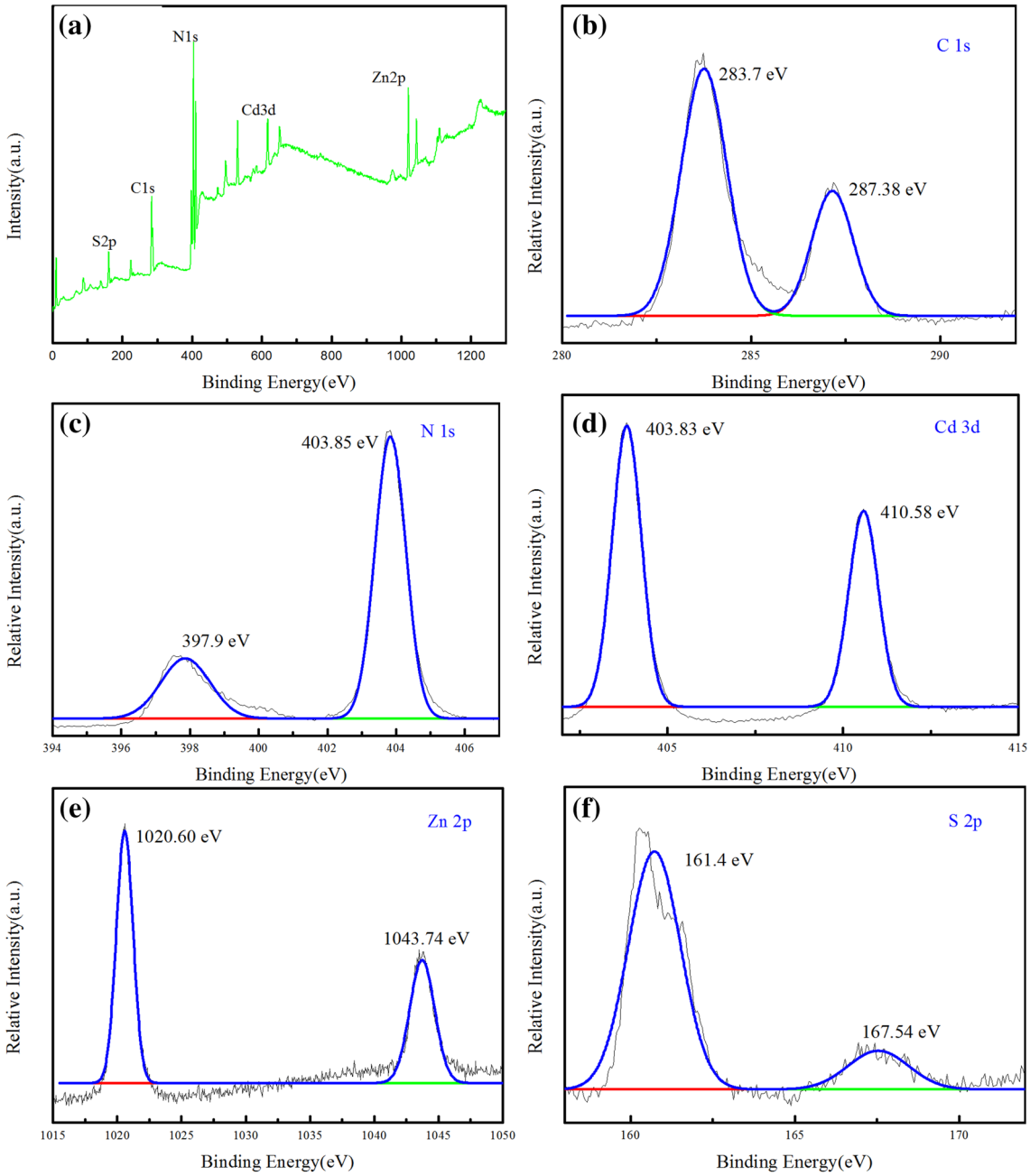

Fig. 5 FT-IR spectra of 50-CN@ZCS: **a** survey; **b** C 1 *s*; **c** N 1 *s*; **d** Cd 3*d*; **e** Zn 2*p*; **f** S 2*p*

band edges of all the prepared CN@ZCS heterojunctions are located between them. With the composite ratio of g-C_3N_4 increasing, the absorption band edge shifts to blue, and the color of the CN@ZCS change from yellow to white. Combined with the TEM analysis, it can be concluded that the g-C_3N_4 and $Zn_{0.5}Cd_{0.5}S$ can form a stable heterojunction structure. According to the Kubelka–Munk function method [35], the band gap of light energy can be calculated by $h\upsilon$ and $[F(R)\cdot h\upsilon]^{0.5}$, and the result is shown in Fig. 8b. The band gap of $Zn_{0.5}Cd_{0.5}S$ is 2.5 eV. The absorption intensity of the CN@ZCS heterojunction in the visible light range is higher than that of g-C_3N_4, and the bandgap width increases with increasing the g-C_3N_4 content. It is concluded that the prepared CN@ZCS heterojunction absorbes more light than g-C_3N_4, which is beneficial to produce more electron–hole pairs.

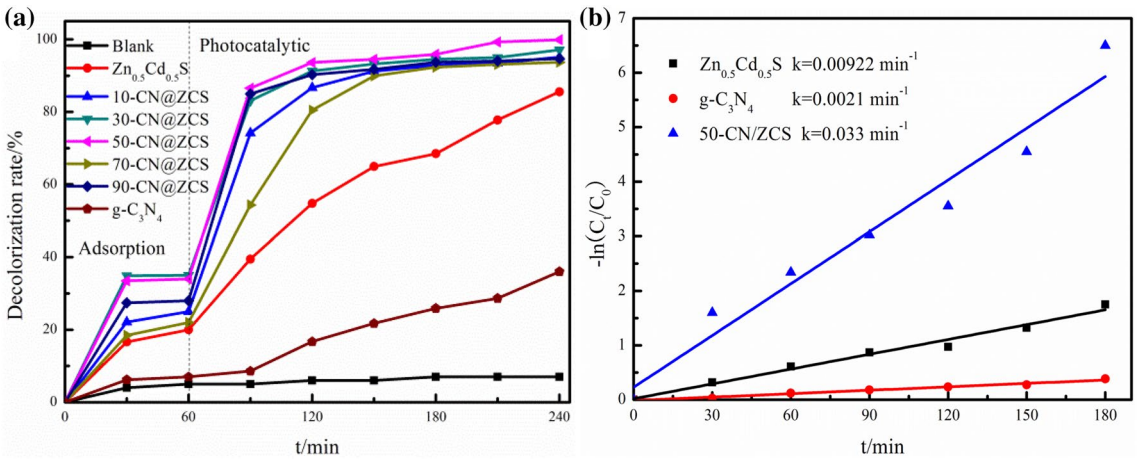

Fig. 6 **a** Photocatalytic efficiency and **b** kinetic analysis of CN@ZCS with different mass ratios

4.4 Photoelectric property analysis

The photoactivity of a semiconductor is usually affected by the separation efficiency of the photo-generated carriers. The transient photocurrent response is measured at a specific time interval of the xenon illumination. As shown in Fig. 9a, the increasing transient photocurrent of 50-CN@ZCS is ascribed to the irradiation of visible light, and the generation and separation of electron–hole pairs forming a stable current. The 50-CN@ZCS heterojunction structure increases the separation efficiency of the photogenerated carriers, while the photocurrent response of g-C_3N_4 is very low.

Electrochemical impedance spectroscopy (EIS) is an effective method to study the interfacial reaction process of materials. Figure 9b shows the electrochemical impedance spectrum of g-C_3N_4, $Zn_{0.5}Cd_{0.5}S$ and 50-CN@ZCS. Compared to g-C_3N_4 and $Zn_{0.5}Cd_{0.5}S$ the Nyquist circle radius of the 50-CN@ZCS heterojunction decreases, and the Nyquist circle radius of g-C_3N_4 is higher. This indicates that the contact resistance and transmission resistance of the 50-CN@ZCS heterojunction surface are reduced. The faster charge transfer on the 50-CN@ZCS heterojunction surface makes the faster photogenerated electron–hole separation [36].

4.5 Photoluminescence spectrum

The semiconductor produces an electron (e^-) and hole (h^+) separation during light excitation, but the photoelectron and hole easily recombine and produce optical signal. Therefore, the photoluminescence spectroscopy (PL) is used to determine the electron–hole recombination probability of each sample under 325 nm photoexcitation, as shown in Fig. 10. The fluorescence emission peaks of the g-C_3N_4 and $Zn_{0.5}Cd_{0.5}S$ are around 460 nm and 550 nm. The fluorescence emission peak intensity of the CN@ZCS heterojunction is lower than that of g-C_3N_4. With the increase in the g-C_3N_4 content, the position of the emission peak gradually shifted to 460 nm, indicating that g-C_3N_4 and $Zn_{0.5}Cd_{0.5}S$ formed a heterojunction, and g-C_3N_4 gradually played a leading role [37]. The lowest intensity of the 30-CN@ZCS and 50-CN@ZCS indicates the lowest photogenerated electron–hole recombination probability.

4.6 Capture agent analysis

The active substances play a major role in the degradation of MB by the 50-CN@ZCS catalyst. The capture agent tests were performed to study the active substances of catalyst. The operation method is the same as the photocatalytic experiment. The MB concentration is 20 mg/L, 1 mM TBA, EDTA-2Na, and BQ were added to the reaction system, and the degradation results are shown in Fig. 11. With the addition of TBA, the photocatalytic degradation efficiency slightly decreased, indicating that ·OH plays a minor role in the degradation process. When EDTA-2Na and BQ are added, the photocatalytic degradation efficiency significantly decreased demonstrating that $O_2^{-\cdot}$ is the active substance. As shown in Fig. 11, the valence band potentials of g-C_3N_4 (+1.4 eV) and $Zn_{0.5}Cd_{0.5}S$ (+1.975 eV) are much lower than that of E^0(·OH/OH^-)(2.38 eV) [38]. However, the conduction band potential of g-C_3N_4 (−1.3 eV) and $Zn_{0.5}Cd_{0.5}S$ (−0.525 eV) are both more negative than those of $E^0(O_2/O_2^{-\cdot})$ (−0.28 eV) [39]. Therefore, ·OH cannot be produced, while only $O_2^{-\cdot}$ can be produced. The combination of g-C_3N_4 and $Zn_{0.5}Cd_{0.5}S$ reduces the possibility of photoelectron-hole recombination, allowing a high number of holes and $O_2^{-\cdot}$ to react with MB to improve the photocatalytic efficiency.

Table 1 Comparison of photocatalytic performance of ZnS or CdS dispersed on carbon nitride

Photocatalyst	Preparation	Morphology	Dye [V (mL), C (mg/L)]	Degradation efficiency	Reference
50% $Zn_{0.8}Cd_{0.2}S/g\text{-}C_3N_4$	Hydrothermal method	$Zn_{0.8}Cd_{0.2}S$ nanoparticles are distributed on the surface of flaky $g\text{-}C_3N_4$	100 mL 10 mg/L MB	180 min 98%	[18]
20%$g\text{-}C_3N_4$/ $Zn_{0.25}Cd_{0.75}S$	Hydrothermal method	$Zn_{0.25}Cd_{0.75}S$ nanoparticles are deposited on lamellar $g\text{-}C_3N_4$	80 mL 10 mg/L MO	75 min 98%	[32]
20 wt% $CdS/g\text{-}C_3N_4$	Coprecipitation method	Flaky $g\text{-}C_3N_4$ loaded on the surface of CdS microspheres	50 mL 10 mg/L MO	15 min 97.3%	[40]
73.3% $CdS/g\text{-}C_3N_4$	Coprecipitation method	Granular CdS loaded in flake $g\text{-}C_3N_4$	100 mL 5 mg/L MO	60 min 99%	[16]
10 wt% $g\text{-}C_3N_4$/ZnS	Wet chemical method	Plate-shaped $g\text{-}C_3N_4$ wrapped on the surface of rod-shaped ZnS	60 mL 10 mg/L MO	100 min 93%	[17]
$ZnS@g\text{-}C_3N_4$	In situ thermal polycondensation method	Nanoparticle ZnS is supported on the surface of flake $g\text{-}C_3N_4$	100 mL 10 mg/L RhB	80 min 95.3%	[28]
$g\text{-}C_3N_4$-CdS (1:3)	Coprecipitation method	CdS nanoparticles are randomly distributed in flaky $g\text{-}C_3N_4$	200 mL 25 mg/L MB	180 min 90.45%	[43]
$CdS:g\text{-}C_3N_4 = 0.8:1$	Ultrasonic physical mixing	CdS nanowires are embedded in the $g\text{-}C_3N_4$ nanosheet	100 mL 5 mg/L RhB	180 min 95%	[44]
$g\text{-}C_3N_4$/ZnS/CuS	Ultrasonic ultraviolet light wave synthesis	ZnS nanoparticles are embedded in the surface of hexagonal flake CuS, and CuS is superimposed with microchip $g\text{-}C_3N_4$	100 mL 10 mg/L RhB	90 min 90%	[45]
$CdS\text{-}C_3N_4$	Wet chemical precipitation method	CdS nanoparticles are mainly deposited on the surface of flaky C_3N_4	100 mL 10 mg/L RhB	120 min 97%	[23]
$CdS/g\text{-}C_3N_4$	Assisted ultrasonic stripping method	CdS nanoparticles are evenly distributed on the surface of $g\text{-}C_3N_4$	60 mL 5 mg/L MO	120 min 97%	[46]
$CdS/Au/g\text{-}C_3N_4$	Two-step photoreduction method	Au, CdS nanoparticles are evenly distributed on the surface of $g\text{-}C_3N_4$	100 mL 10 mg/L RhB	30 min 99%	[47]
$CdS/g\text{-}C_3N_4$	Ultrasonic precipitation method	CdS nanoparticles are evenly distributed on the surface of $g\text{-}C_3N_4$	100 mL 4 mg/L RhB	180 min 80%	[48]
$g\text{-}C_3N_4/Co_xMo_{1-x}S_2$	Solvothermal method	$Co_xMo_{1-x}S_2$ sheet and $g\text{-}C_3N_4$ sheet are laminated together to form a multi-layer structure	Hydrogen production	5 h H_2 production 818.6 μmol	[49]
$CdS/g\text{-}C_3N_4$	Hydrothermal method	CdS nanorods are embedded in flaky $g\text{-}C_3N_4$ and entangled to form nanospheres	200 mL 10 mg/L MO	15 min 98%	[50]
$OLC/pg\text{-}C_3N_4$	Ultrasonic adsorption	A great number of OLC nanoparticles around 5 nm were loaded on the surface of $pg\text{-}C_3N_4$	50 ml 5 mg/L RhB, MB, MO or phenol solution	40 min RhB 91% MB 90.05% MO 78.9% phenol solution 38.3%	[51]

Table 1 (continued)

Photocatalyst	Preparation	Morphology	Dye [V (mL), C (mg/L)]	Degradation efficiency	Reference
CNTs/$Bi_{12}O_{17}Cl_2$	Hydrothermal method	The tubular CNTs are tightly bonded to the surface of the flaky $Bi_{12}O_{17}Cl_2$	50 mL 5 mg/L RhB	25 min 78%	[52]
g-C_3N_4@$Zn_{0.5}Cd_{0.5}S$	Coprecipitation-hydrothermal method	CdS wrapped on the surface of g-C_3N_4 to form a core–shell structure	100 mL 10 mg/L MB	120 min 95.54%	This work

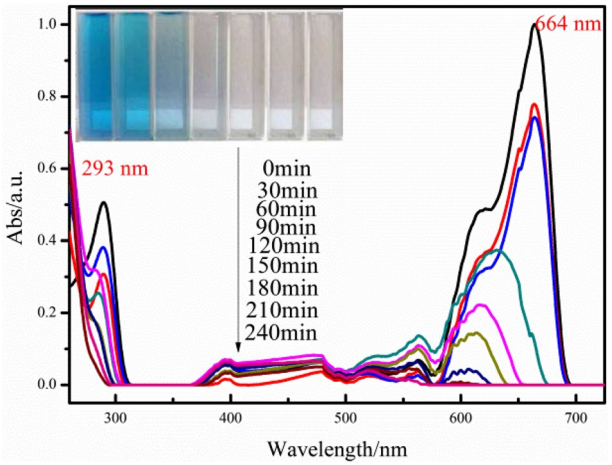

Fig. 7 Temporal UV–Vis absorption spectral changes during the photo-degradation of MB using 50-CN@ZCS

The valence band level (E_{CB}) of a semiconductor can be calculated from the empirical formula $E_{CB}=X-E_C-Eg/2$ [40] (X is the geometric mean electronegativity of semiconductors; E_C is a constant relative to the standard H electrode with a value of 4.5 eV; E_{CB} is the conduction potential of the conduction band; and Eg is the forbidden band width of the semiconductor). By calculation, the VB and CB of g-C_3N_4 are 1.4 eV and − 1.3 eV, respectively. The VB and CB of the $Zn_{0.5}Cd_{0.5}S$ are 1.975 eV and − 0.525 eV, respectively. Therefore, their energy levels match well. As shown in Fig. 12, when a heterojunction is formed between g-C_3N_4 and $Zn_{0.5}Cd_{0.5}S$, the photoelectron energy rapidly transfers from the surface of g-C_3N_4 to $Zn_{0.5}Cd_{0.5}S$ and the holes aggregate from $Zn_{0.5}Cd_{0.5}S$ to g-C_3N_4 under the action of potential difference driving force. After the redistribution of electrons and holes, a stable internal electric field will be established at the heterogeneous interface between the two components, which will inhibit the electron–hole recombination process and greatly improve the photocatalytic performance. Photogenerated electrons (e^-) are transferred to the surface of $Zn_{0.5}Cd_{0.5}S$ and combine with O_2 to form superoxide anions ($O_2^{-\cdot}$), and finally h^+ and $O_2^{-\cdot}$ degrade the methylene blue dye into CO_2 and H_2O [41]. The main chemical reactions are as the follows (1–4):

$$g\text{-}C_3N_4/Zn_{0.5}Cd_{0.5}S + h\upsilon \rightarrow h^+(g\text{-}C_3N_4) + e^-(Zn_{0.5}Cd_{0.5}S) \quad (1)$$

$$O_2 + e^-(Zn_{0.5}Cd_{0.5}S) \rightarrow O_2^{-\cdot} \quad (2)$$

$$O_2^{-\cdot} + MB \rightarrow \text{degradation products} \quad (3)$$

$$MB + h^+ \rightarrow \text{degradation products} \quad (4)$$

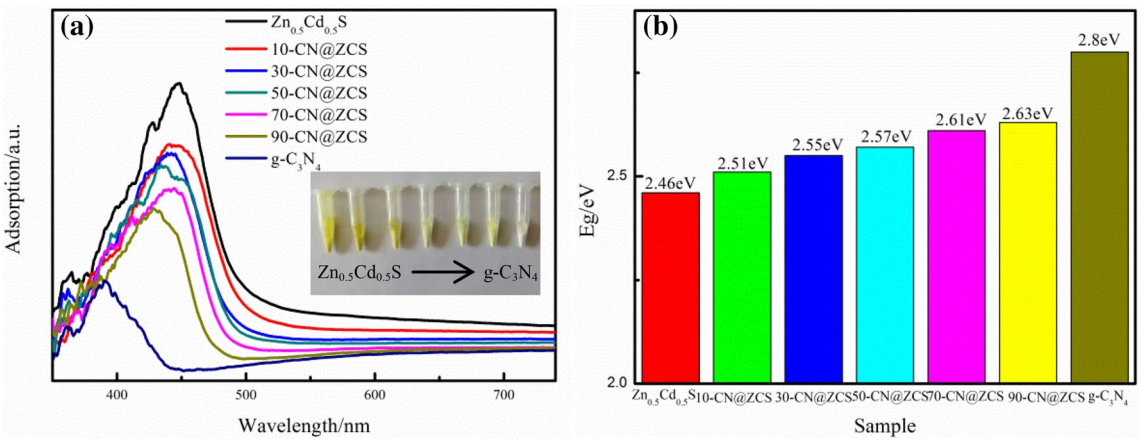

Fig. 8 **a** UV–Vis DRS spectrums of CN@ZCS, **b** The Eg of CN@ZCS with the g-C_3N_4 content

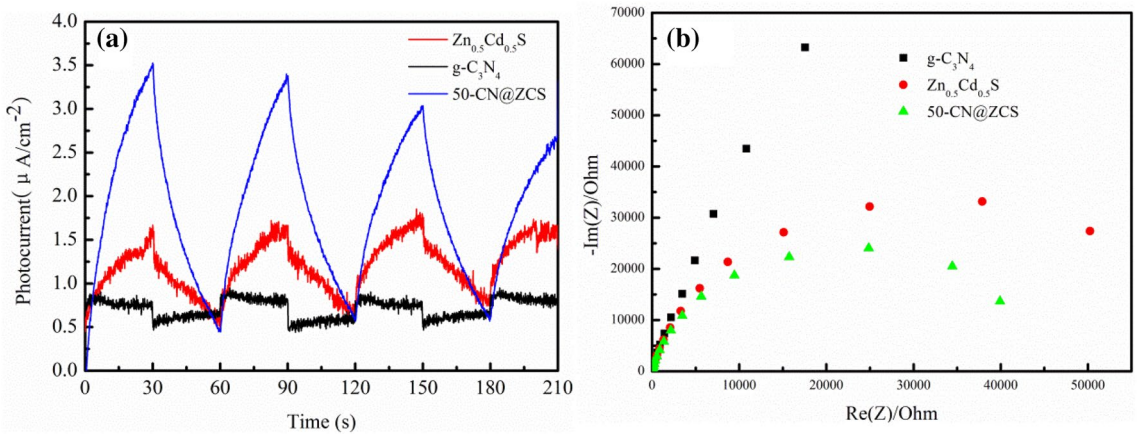

Fig. 9 **a** Transient photocurrent response and **b** the corresponding electrochemical impedance spectroscopy of g-C_3N_4, $Zn_{0.5}Cd_{0.5}S$ and 50-CN@ZCS

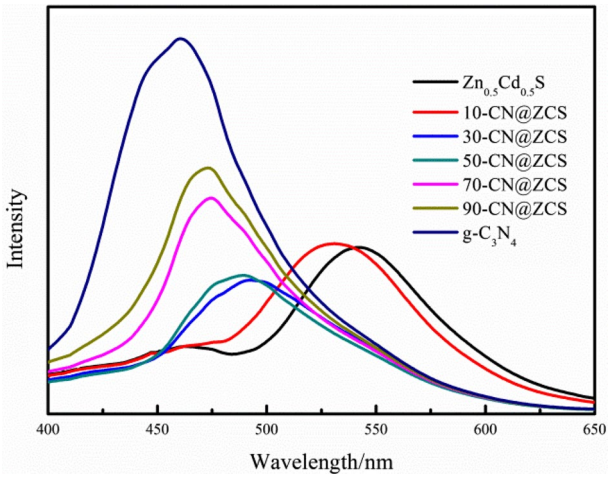

Fig. 10 PL spectra of different quality ratios of CN@ZCS

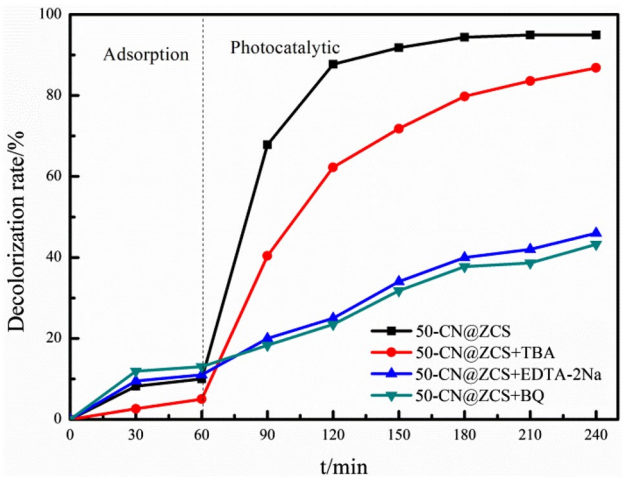

Fig. 11 The capture agent experiment for the 50-CN@ZCS catalyst

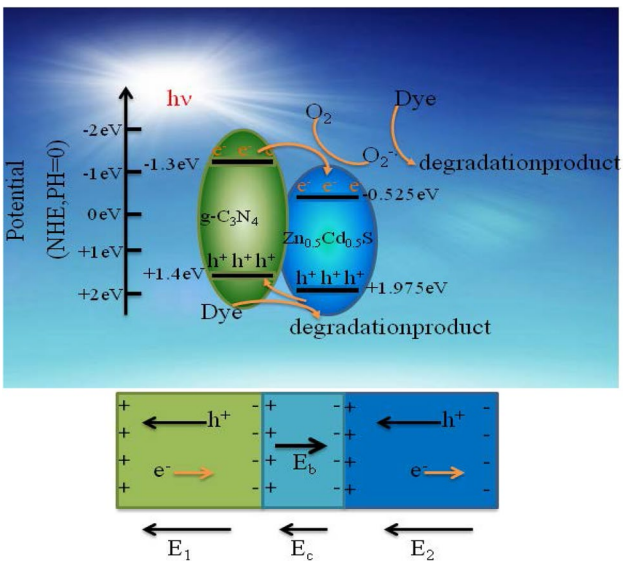

Fig. 12 Schematic illustration of electron–hole separation and transport at the g-C_3N_4/$Zn_{0.5}Cd_{0.5}S$ heterojunction interface. E_c is the contact electric field; E_b is the barrier in the interface depletion layer; and E_1 and E_2 are the internal electric fields caused by the spatial charge redistribution in g-C_3N_4 and $Zn_{0.5}Cd_{0.5}S$, respectively

4.7 Stability analysis of photocatalyst

Recycling of the photocatalyst is a crucial step in the actual photocatalysis process [42]. The degradation rate of MB is shown in Fig. 13a, and the photocatalyst still maintains a high activity (95.7%) after the four successive photocatalytic tests. Figure 13b shows that the chemical structure of 50-CN@ZCS does not change after four photocatalytic cycles. Figure 13c shows the UV–Vis diagram of the 50-CN@ZCS photocatalytic degradation of MB. 50-CN@ZCS does not significantly change in the light absorption

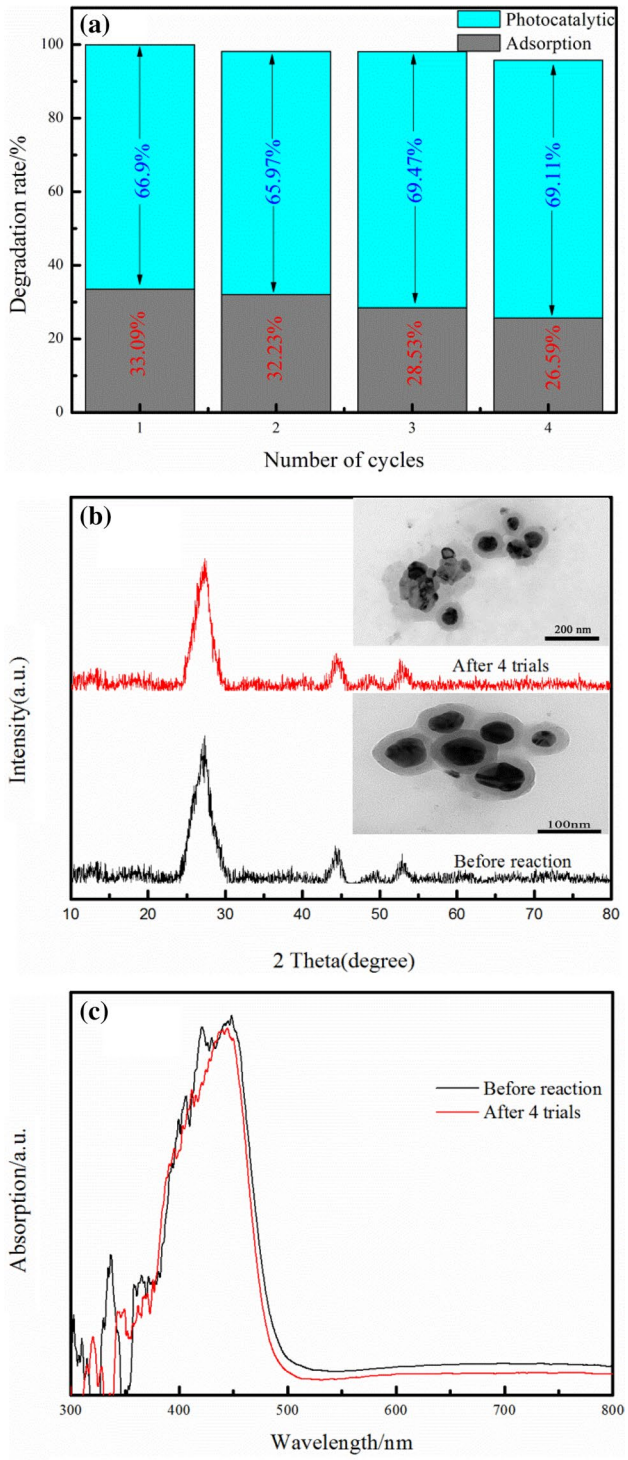

Fig. 13 **a** Photocatalytic degradation rate of MB by 50-CN@ZCS after four cycles; **b** XRD and TEM comparison chart of 50-CN@ZCS after four cycles; **c** UV–Vis comparison chart of 50-CN@ZCS after four cycles

band after the photocatalytic degradation. Therefore, it can be seen that the 50-CN@ZCS core–shell heterojunction has an excellent light stability.

5 Conclusion

In this study, a simple co-precipitation-hydrothermal method was used to synthesize a photocatalyst of the g-C_3N_4@$Zn_{0.5}Cd_{0.5}S$ heterojunction. This core–shell structure enhances the visible light response range, facilitates the separation migration of photogenerated carriers, and improves the activities and stabilities. The photocatalytic performance of the 50-CN@ZCS heterojunction is much higher than those of g-C_3N_4 and $Zn_{0.5}Cd_{0.5}S$. The decolorization rate of MB can reach 99.9% in 240 min and the rate constant is 0.033 min^{-1}, which is 3.6 times and 15.7 times higher than those of g-C_3N_4 and $Zn_{0.5}Cd_{0.5}S$, respectively. The photocatalytic activity remains at 65% after 4 cycles. The main active substances are h^+ and $O_2^{-\cdot}$ in the degradation process.

Acknowledgements The project was supported by National Youth Fund Project of China (Grant No. 51404083).

References

1. J. Chen, B.B. Ding, T.Y. Wang, F. Li, Y. Zhang, Y.L. Zhao, H.S. Qian, J. Mater. Sci. **25**, 4103–4109 (2014)
2. J. Yan, K. Wang, H. Xu, J. Qian, W. Liu, X. Yang, H. Li, Chin. J. Catal. **34**, 1876–1882 (2013)
3. L. Li, S. Xue, P. Xie, H. Feng, X. Hou, Z. Liu, R. Zou, Electron. Mater. Lett. **14**, 739–748 (2018)
4. D. Zewde, O.P. Yadav, A.M. Taddesse, Curr. Phys. Chem. **7**, 172–180 (2017)
5. C. Zhang, H. Liu, W. Wang, H. Qian, S. Cheng, Y. Wang, Y. Hu, Appl. Catal. B **239**, 309–316 (2018)
6. A.G. Kyazym-zade, M.A. Jafarov, E.F. Nasirov, C.A. Jahangirova, R.S. Jafarli, Semiconductors **51**, 454–457 (2017)
7. H.F. Ye, R. Shi, X. Yang, W.F. Fu, Y. Chen, Appl. Catal. B **233**, 70–79 (2018)
8. M. Askari, N. Soltani, E. Saion, W.M.M. Yunus, H.M. Erfani, M. Dorostkar, Superlattices Microstruct. **81**, 193–201 (2015)
9. W. Wang, W. Zhu, H. Xu, J. Phys. Chem. C **112**, 16754–16758 (2008)
10. J. Zhang, W.N. Wang, M.L. Zhao, C.Y. Zhang, C.X. Huang, S. Cheng, H.S. Qian, Langmuir. **34**, 9264–9271 (2018)
11. W.J. Ong, L.L. Tan, Y.H. Ng, S.T. Yong, S.P. Chai, Chem. Rev. **116**(12), 7159–7329 (2016)
12. L. Yang, J. Huang, L. Shi, L. Cao, Q. Yu, Y. Jie, J. Ye, Appl. Catal. B **204**, 335–345 (2017)
13. F. Wang, P. Chen, Y. Feng, Z. Xie, Y. Liu, Y. Su, G. Liu, Appl. Catal. B **207**, 103–113 (2017)
14. Z. Li, Q. Zhang, X. He, M. Chen, Appl. Clay. Sci. **151**, 201–210 (2018)
15. H. Wu, Y. Yao, W. Li, L. Zhu, N. Ni, X. Zhang, Mol. Microbiol. Biotechnol. **13**, 2225–2234 (2011)
16. H. Xu, L. Wu, L. Jin, K. Wu, J. Mater. Sci. Technol. **33**, 30–38 (2017)
17. Q. Wang, Y. Shi, Z. Du, J. He, J. Zhong, L. Zhao, B. Su, Eur. J. Inorg. Chem. **2015**, 4108–4115 (2015)
18. D. Li, Z. Wu, C. Xing, D. Jiang, M. Chen, W. Shi, S. Yuan, J. Mol. Catal. A **395**, 261–268 (2014)

19. Y.X. Dong, J.T. Cao, B. Wang, S.H. Ma, Y.M. Liu, ACS Appl. Mater. Interface **10**, 3723–3731 (2018)
20. L.C. Wu, H.Y. Xu, H. Zhao, Appl. Mech. Mater. **618**, 215–219 (2014)
21. J.Y. Zhang, Y.H. Wang, J. Jin, J. Zhang, Z. Lin, F. Huang, J. Yu, ACS Appl. Mater. Interface **5**, 10317–11032 (2013)
22. U. Mizutani, MRS Bull. **37**, 169–169 (2012)
23. R.G. Chaudhuri, A. Chaturvedi, E. Iype, Mater. Res. Express. **5**, 036202 (2018)
24. Y. Deng, L. Tang, G. Zeng, Z. Zhu, M. Yan, Y. Zhou, J. Wang, Appl. Catal. B **203**, 343–354 (2017)
25. J. Wen, J. Xie, X. Chen, X. Li, Appl. Surf. Sci. **391**, 72–123 (2017)
26. W.K. Jo, N.C.S. Selvam, Chem. Eng. J. **317**, 913–924 (2017)
27. Z. Qian, H. Shaozheng, L. Fayun, F. Zhiping, W. Qiong, W. Fei, L. Daosheng, Chem. J. Chin. U. **37**, 521–528 (2016)
28. B. Xue, H.Y. Jiang, T. Sun, F. Mao, Catal. Lett. **146**, 2185–2192 (2016)
29. J. Feng, T. Chen, S. Liu, Q. Zhou, Y. Ren, Y. Lv, Z.J. Fan, J. Colloid Interface Sci. **479**, 1–6 (2016)
30. Y.G. Li, X.L. Wei, H.J. Li, R.R. Wang, J. Feng, H. Yun, A.N. Zhou, RSC Adv. **5**(1), 14074–14080 (2015)
31. H. Li, J. Li, C. Xu, P. Yang, D.H. Ng, P. Song, M. Zuo, J. Alloys Compd. **698**, 852–862 (2017)
32. X. Liu, W. Yang, C. Yu, H. Zhang, J. Environ. Chem. Eng. **6**(4), 4899–4907 (2018)
33. X. Liang, P. Wang, M. Li, Q. Zhang, Z. Wang, Y. Dai, B. Huang, Appl. Catal. B **220**, 356–361 (2018)
34. X. Liu, P. Lv, G. Yao, C. Ma, Y. Tang, Y. Wu, Y. Yan, Colloids Surf. A **441**, 420–426 (2014)
35. W. Wang, S. Li, C. Pan, S. Liu, T. Luo, G. Dai, J. Chin. Chem. Soc. **65**, 252–258 (2018)
36. Y. Bai, L. Ye, T. Chen, L. Wang, X. Shi, X. Zhang, D. Chen, ACS Appl. Mater. Interface **8**, 27661–27668 (2016)
37. Q. Nie, Q. Yuan, Q. Wang, Z. Xu, J. Mater. Sci. Lett. **39**, 5611–5612 (2004)
38. Q. Liu, C. Fan, H. Tang, X. Sun, J. Yang, X. Cheng, Appl. Surf. Sci. **358**, 188–195 (2015)
39. X.H. Yang, H.T. Fu, X.Z. An, X.C. Jiang, A.B. Yu, RSC Adv. **6**, 34103–34109 (2016)
40. J. Cao, B. Luo, H. Lin, B. Xu, S. Chen, J. Hazard. Mater. **217**, 107–115 (2012)
41. C. Zhang, Y. Lu, Q. Jiang, J. Hu, Nanotechnology. **27**, 355402 (2016)
42. M. Sun, T. Yan, Q. Yan, H. Liu, L. Yan, Y. Zhang, B. Du, RSC Adv. **4**, 19980–19986 (2014)
43. F. Jiang, T. Yan, H. Chen, A. Sun, C. Xu, X. Wang, Appl. Surf. Sci. **295**, 164–172 (2014)
44. Y. Xu, W.D. Zhang, Eur. J. Inorg. Chem. **2015**, 1744–1751 (2015)
45. Y. Sun, J. Jiang, Y. Cao, Y. Liu, S. Wu, J. Zou, Mater. Lett. **212**, 288–291 (2018)
46. L. Zhang, F. Huang, C. Liang, L. Zhou, X. Zhang, Q. Pang, J. Taiwan Inst. Chem. Eng. **60**, 643–650 (2016)
47. D. Peng, H. Wang, K. Yu, Y. Chang, X. Ma, S. Dong, RSC Adv. **6**, 77760–77767 (2016)
48. D. Wang, Z. Xu, Q. Luo, X. Li, J. An, R. Yin, C. Bao, J. Mater. Sci. Lett. **51**, 893–902 (2016)
49. X. Hao, Z. Jin, S. Min, G. Lu, RSC Adv. **6**, 23709–23717 (2016)
50. Z.L. Fang, H.F. Rong, L.Y. Zhou, P. Qi, J. Mater. Sci. **50**, 3057–3064 (2015)
51. L. Shi, F. Wang, J. Zhang, J. Sun, Ceram. Int. **42**, 18116–18123 (2016)
52. L. Shi, J. Ma, L. Yao, L.S. Cui, W. Qi, J Colloid Interface Sci. **519**, 1–10 (2018)